Tensile deformation of a Ti-based metallic glass composite lamella confined by commercially pure titanium

F. F. Wu[a,b], K. C. Chan[a *], S. T. Li[b], G. Wang[c] and P. Lin[d]

[a]*Advanced Manufacturing Technology Research Centre, Department of Industrial and Systems Engineering, Hong Kong Polytechnic University, Kowloon, Hong Kong, China*

[b]*School of Materials Science and Engineering, Liaoning University of Technology, Jinzhou 121001, China*

[c]*Laboratory for Microstructures, Shanghai University, Shanghai200444, China*

[d]*School of Materials Science and Engineering, Harbin Institute of Technology, Harbin 151001, China*

ABSTRACT

The tensile plastic deformation behavior of a Ti-based metallic glass composite (MGC) lamella confined by commercially pure titanium (CPT) is investigated. It is found that a uniform plastic deformation is achieved in the CPT-confined MGC lamella, where the strain localization and necking is effectively suppressed. The MGC lamella sustains a true tensile strain exceeding 10% before fracture. A deformation mechanism of the amorphous/crystalline interface is proposed to interpret the plastic deformation of the MGC/CPT structure. The revealed significant intrinsic plasticity of the MGC suggests its potential application as an excellent coating for bulk ductile materials.

Keywords: Metallic glass; tensile plasticity; plastic deformation; fracture

*Corresponding author. Email: mfkcchan@inet.polyu.edu.hk

1. Introduction

Extensive investigations over the past years have indicated that the strength of metallic glasses (MGs) is high on account of the absence of crystalline defects, but at the expense of tensile ductility [1-5]. The lack of plastic deformation in MGs is attributed to a very localized shear banding behavior [1-5]. However, on the micron scale, the shear strain in one of the shear bands of a MG is believed to be as large as 10^2 or more [6]. Therefore, MGs should be intrinsically ductile at the micron scale, which has been verified by a few reports on the mechanical behavior of MGs with size decreasing to the micrometer or nanometer scale [5, 7-10]. According to this understanding, introducing an inhomogeneous phase, such as body-centered cubic β-dendrite, to tailor the glassy phase with several patches at the micron size may effectively inhibit the unstable and fast propagation of single shear bands, and subsequently activate multiple shear bands in the MG matrix, which could significantly improve the ductility of MG composites (MGC) [11-13]. However, MGCs exhibit two different types of plastic deformation. In tensile deformation, they usually show an inhomogeneous deformation mode: strong necking or strain localization after yielding. Once MGCs are subjected to a compressive load, a large plastic strain can be obtained [11, 14-16]. On the other hand, the fracture surface of β-dendrite-reinforced MGCs shows many fine vein patterns with a profusion of short shear bands formed in the necking region, indicating a substantial degree of plastic deformation prior to failure [11-13]. Thus, based on previous studies, we conclude that the limited tensile ductility or homogeneous plastic deformation capability of MGCs can be attributed to both an absence of work-hardening of the MG matrix and a weak work-hardening ability of the β-dendrites. So, uniform tensile plastic deformation

cannot be achieved owing to strain localization and early necking and, therefore, strain localization must be effectively suppressed in order to achieve an intrinsic tensile plasticity for MGC samples.

Some investigations have shown that the confinement exerted by a ductile substrate can suppress the inhomogeneous plastic deformation in nanocrystalline metallic materials under tension [17-19]. Accordingly, it is expected that a large homogeneous plastic deformation could be achieved if the strain localization in the MGC could be effectively suppressed by a ductile substrate. In this method of improving the ductility of MGCs by exerting confinement, the elastic mismatch and the interface bonding between the MGC and the matrix are two important parameters [17-19].

In this work, a β-dendrite-reinforced Ti-based MGC was chosen as the model material. An ideal structure, i.e. a MGC sheet metallurgically bonded to a commercially pure titanium (CPT), was produced by re-melting a β-dendrite-reinforced Ti-based MGC on a commercially pure titanium sheet surface. This designed MGC/CPT structure can produce a nice interface bonding between the MGC and the CPT, and display different mechanical responses, providing an opportunity to reveal the uniform tensile plastic deformation of a MGC without strain localization, and to achieve a large uniform tensile plasticity in an MGC confined by CPT.

2. Experimental

The β-dendrite-reinforced Ti-based MGC, with chemical composition $Ti_{43}Zr_{27}Mo_5Cu_{10}Be_{15}$, was prepared by arc melting and cast in a copper mold. The MGC was

then cut into a sheet with dimensions 30 × 10 × 1 mm^3 (length×width×thickness), and put on the CPT sheet with dimensions 30 × 10 × 2 mm^3 (length×width×thickness) preset on a water-cooled copper base. The MGC sheet was then re-melted on the CPT sheet by an argon arc. The current and voltage applied in the argon arc were 200 A and 30 V respectively. The distance between the tungsten electrode and the MGC sheet was about 10 mm. Finally, 30×10×3 mm^3 MGC/CPT bimetallic sheets were manufactured. The process of the fabrication of these bimetallic sheets is schematically shown in Figure 1a. All the manipulation described above was conducted in a vacuum arc furnace. The phases of the MGC ingots and MGC/CPT bimetallic sheets were characterized by X-ray diffraction (XRD) using a Rigaku diffractometer with Cu K_α radiation. The microstructure and chemical composition were examined by a Hitachi 3000S scanning electronic microscope (SEM) and optical observations were conducted using a Carl Zeiss microscope. The tensile samples of the monolithic MGC (labelled sample S1), the CPT substrate, and the MGC/CPT bimetallic sheet (labelled sample S2), with gauge dimensions 8 × 1 mm^2 (length×width), were prepared using an electric spark. The MGC sheet in the tensile sample was ground and finally polished to be about 200 μm in thickness. The CPT substrate in the tensile sample was finally polished to 2 mm in thickness. The tensile tests were conducted with a MTS810 testing machine at room temperature using a constant strain rate of 1 × 10^{-4} s^{-1}. Each experiment was repeated five times. The deformed samples were investigated by SEM to reveal deformation and fracture features.

3. Results and discussion

Figure 1b shows the microstructure of the bimetallic sheet: the top layer is the

β-dendrite-reinforced Ti-based MGC, and the lower substrate is the CPT. The interfacial layer between the MGC and CPT is a β-Ti alloy with a body-centered cubic (bcc) structure, which is similar to the β-dendrites in the MGC (see Figure 1c). The XRD pattern of the top layer showed that the dendrite is a bcc lattice and the matrix is an amorphous structure (Figure 1e). The secondary dendrite arm is about 5 μm on average (see Figure 1d). The volume fraction of the β dendrites is about 54%, measured from the SEM image. Based on the measurements of the energy-dispersive X-ray spectrum (EDS), the chemical compositions of the β-dendrites and the amorphous matrix are $Ti_{65.4}Zr_{19.3}Mo_{9.7}Cu_{5.6}$ and $Ti_{24.8}Zr_{32.7}Mo_{0.9}Cu_{14.1}Be_{27.5}$ respectively. The grain size of the close-packed hexagonal α-CPT substrate is about 150 μm.

The results of quasi-static tensile tests of the Ti-based MGC show a yield strength of 1756 ± 50 MPa, and zero uniform elongation, with a remarkable necking or strain localization, as shown in S1 of Figure 2. Such a high yield strength and severe strain localization tensile behavior of the present MGC are analogous to those of other β-dendrite-reinforced MGCs described in the literature [11-13]. The calculated reduction of area in the fracture region was close to 49.9%, and the corresponding local engineering and true strains were about 99.7% and 0.692, respectively. Therefore, it is obvious that the MGC exhibits a very high plastic deformation, but the plastic flow proceeded unstably after yielding. The estimated failure strength in the necking fracture cross-section was about 2465 ± 60 MPa, which is almost 39% higher than its yield strength of 1756 ± 50 MPa. This indicates that work hardening still occurs in the whole plastic deformation process, but it cannot counterbalance the load capacity decrease induced by the narrowing of the tensile sample [11-13].

When the MGC is confined by the CPT substrate, its plastic deformation behavior is

quite different from a monolithic sample. Considering a relatively homogeneous deformation in the bimetal, the rule of mixtures is used to predict the strength of the bimetallic sheet. The stress-strain curve of S2 in Figure 2 plots the CPT-confined MGC's plastic deformation behavior by subtracting the stress-strain behavior of the monolithic CPT, which is calculated from

$$\sigma_{\mathrm{MGC}} = \frac{\sigma_{\mathrm{MGC/CPT}} - V_{\mathrm{CPT}}\sigma_{\mathrm{CPT}}}{V_{\mathrm{MGC}}}. \quad (1)$$

Here, σ_{MGC}, σ_{CPT}, $\sigma_{\mathrm{MGC/CPT}}$ are the stresses of the MGC in the MGC/CPT bimetal, the monolithic CPT, and the MGC/CPT bimetal, respectively. V_{CPT} and V_{MGC} are the volume fractions of the CPT and MGC in the MGC/CPT bimetal, respectively. It is clear that an MGC confined by CPT can homogeneously deform, approaching the plastic strain of about 13.2%, which is unusually found in these dendrite-reinforced MGC, where obvious work hardening occurs. The yield stress is almost the same as that of the monolithic MGC and the maximum strength reaches about 2300 MPa. The inset of Figure 2 shows comparatively the shapes of the fractured monolithic MGC and the fractured MGC confined by the CPT. It is evident that the monolithic MGC shows a significant necking behavior while no obvious necking can be observed in the sample confined by the CPT, even in the fracture region

The fractured samples were further observed by SEM. It is noted that the the MGC confined by CPT is elongated homogeneously (Figure 3a). By close examination of the deformation morphology, two positions in the centre and outskirts of sample S2 are representatively shown in Figure 3b and 3c. The surface of the deformed MGC/CPT exhibits multiple short and tiny shear bands that are produced on the metallic glass matrix. The dendrites also underwent large deformation with profuse shear bands on the surface (Figure

3b and 3c). No penetrative major shear bands and obvious microcracking was found in the deformed MGC layer (Figure 3b and 3c) [4]. In contrast to the severe strain localization of the monolithic MGC, quasi-static tension of the MGC/CPT samples showed that the MGC layer deforms coherently with the CPT substrate, as shown in Figure 3d and 3e. No surface cracking or delamination was observed between the MGC layer and the CPT substrate, even in the necking region at failure. From five tensile tests, uniform elongation of the MGC/CPT samples was observed, which was very similar to that of the CPT tensile sample, demonstrating that the strain localization in the MGC layer under tension can be completely suppressed by the CPT substrate. The confined MGC layer exhibits a homogeneous tensile plasticity comparable to the CPT substrate.

Figure 4a plots the stress-strain curve of the MGC/CPT, which shows four deformation stages: (I) linear elastic deformation of the MGC/CPT; (II) partially plastic deformation of the CPT substrate; (III) fully plastic deformation of both the MGC layer and the CPT substrate; (IV) strain localization and fracture. In stage I, the Young's modulus of the MGC/CPT bimetal can be expressed as

$$E_{\mathrm{MGC/CPT}} = V_{\mathrm{MGC}} E_{\mathrm{MGC}} + V_{\mathrm{CPT}} E_{\mathrm{CPT}}, \tag{2}$$

where E_{MGC}, and E_{CPT} are the Young's moduli of the monolithic MGC and the monolithic CPT, respectively. The calculated $E_{\mathrm{MGC/CPT}}$ is about 106 GPa, which is very close to that measured by the stress-strain curve. In stage II, the CPT yields at first, but the MGC still deforms elastically. Therefore，the yield strength of the MGC/CPT bimetal can be calculated as

$$\sigma_y^{\mathrm{MGC/CPT}} = V_{\mathrm{MGC}} \sigma_A^{\mathrm{MGC}} + V_{\mathrm{CPT}} \sigma_y^{\mathrm{CPT}}. \tag{3}$$

Here $\sigma_y^{\mathrm{MGC/CPT}}$ is the yield strength of the MGC/CPT bimetal, σ_y^{CPT} the yield strength of the CPT layer, and σ_A^{MGC} the elastic stress of the MGC layer. Owing to the fact that the MGC layer is still in an elastic state, equation 3 can be rewritten as

$$\begin{aligned}\sigma_y^{\mathrm{MGC/CPT}} &= V_{\mathrm{MGC}} E_{\mathrm{MGC}} \varepsilon_A + V_{\mathrm{CPT}} \sigma_y^{\mathrm{CPT}} \\ &= V_{\mathrm{MGC}} E_{\mathrm{MGC}} (\sigma_y^{\mathrm{CPT}} / E_{\mathrm{CPT}}) + V_{\mathrm{CPT}} \sigma_y^{\mathrm{CPT}}\end{aligned} \tag{4}$$

Considering the small difference of elastic modulus between the MGC and CPT layers, i.e. $E_{\mathrm{MGC}} \approx E_{\mathrm{CPT}}$, equation 4 can be simplified as

$$\sigma_y^{\mathrm{MGC/CPT}} \approx \sigma_y^{\mathrm{CPT}} . \tag{5}$$

This means that the yield strength of the MGC/CPT bimetal is approximately the same as that of the monolithic CPT. The measured $\sigma_y^{\mathrm{MGC/CPT}}$ and σ_y^{CPT} are 429 + 10 MPa and 432 ± 10 MPa, respectively. In this stage, the stress is monotonically increased, which is typical for the plastic deformation of the CPT substrate, as shown in Figure 4b. In stage III, the curve is increased generally, but some stress drop is detected. The stress drop should be attributed to the formation of shear bands and propagation of the MGC layer. The stress increase is caused by the CPT substrate. From Figure 4b, it can be seen that, in the initial plastic deformation of the MGC, the probability of stress drop events (P_{sd}) is very small, namely only one eighth of the probability of the stress increase events (P_{si}). This implies that the shear-banding-induced stress decrease was strongly compensated by the work hardening of the CPT substrate. We can also see from the stress-strain curve that each stress drop is very small, and is attributed to the tailoring of the penetrative major shear band by the β-dendrites of the MGC. With further plastic deformation straining into range III (as marked in Figure 4a), the ratio of the stress drop to stress increase events goes down to $P_{\mathrm{sd}}/P_{\mathrm{si}} = 0.40$ - larger than $P_{\mathrm{sd}}/P_{\mathrm{si}} = 0.13$ in Figure 4b (Figure 4c). Once the stress decrease and increase reach a balance, then the stress decrease

controls the deformation, as shown in Figure 4d for stage IV. However, stage III of the MGC/CPT is very different from that of the monolithic MGC, i.e. the softening rate of the former is smaller than that of the latter, as shown in Figure 2. This indicates that the homogeneous plastic deformation of MGCs is greatly improved through effectively controlling the shear banding of the MG matrix by the confinement of the CPT.

In this MGC/CPT bimetallic composite, dislocations can pile up at the crystalline/amorphous interface, which may trigger a shear band in the amorphous layer when the stress concentration at the tip of a pileup reaches the critical yield shear stress [20]. Usually, the pileup is confined homogeneously in a region of the order of micrometers along the interface, as can be seen indirectly from the slip line of the β-interface in Figure 3e. With the dislocation activity in the CPT substrate, the load is transferred to the elastically deforming glassy matrix of the MGC. As the CPT substrate work hardens, the local stress at the dislocation pileups can be increased to a critical level, which will initiate the shear transformation zones and shear bands in the metallic glass. Thus, a relatively high work hardening rate of the CPT stabilizes the plastic flow of the MGC/CPT such as to allow synchronous deformation. In order to ensure strain compatibility at the MGC/CPT interface, the dislocation-governed slip in the CPT substrate must be matched by the shear banding in the MGC layer. It is of interest to know how the dislocations that arrive at the interface in the CPT substrate are accommodated in the MGC's amorphous phase [20-22]. Uniformly spaced dislocation arrays are formed at the interface when glide dislocations on closely spaced planes impinge on the MGC/CPT interface. Furthermore, shear bands are nucleated in the glassy matrix of the MGC layer when the shear stress is transferred to the elastically deformed MGC

and the local stress reaches the yield shear stress level. At relatively low temperature, these shear transformation zones are nucleated in regions in which there is a critical amount of free volume [23-25]. Thus, a fairly uniform distribution of shear events in the MGC layer is induced by the CPT layer, which provides accommodation for the slipping.

4. Conclusions

In summary, this study demonstrates that MGC are not only strong but also intrinsically ductile as long as strain localization is effectively suppressed. The uniform plastic deformation of the MGC originates from a deformation mechanism of the dislocation pileups, inducing activation of the multiple shear bands in the MGC/CPT interface. The intrinsic mechanical properties of the MGC and the MGC/CPT structures provide a method for enhancing the ductility of MGC materials and imply that MGC layers can be used as advanced coatings for bulk ductile materials.

Acknowledgments

The work described in this paper was supported by the Research Grants Council of the Hong Kong Special Administrative Region, China (Project Nos. PolyU 511510 and PolyU 511211), and the National Natural Science Foundation of China (NSFC) under Grant Nos. 50901038 and 50931005.

References

[1] C.A. Pampillo, J. Mater. Sci. 10 (1975) p.1194.

[2] C.A. Schuh, T.C. Hufnagel and U. Ramamurty, Acta Mater. 55 (2007) p.4067.

[3] W.H. Wang, C. Dong and C.H. Shek, Mater. Sci. Eng. R 44 (2004) p.45.

[4] Z.F. Zhang, F.F. Wu, G. He and J. Eckert, J. Mater. Sci. Technol. 23 (2007) p.747.

[5] J.R. Greer and J.T.M. De Hosson, Prog. Mater Sci. 56 (2011) p.654.

[6] H. Chen, Y. He, G.J. Shiflet and S.J. Poon, Nature 367 (1994) p.541.

[7] C.A. Volkert, A. Donohue and F. Spaepen, J. Appl. Phys. 103 (2008) p.083539.

[8] B.E. Schuster, Q. Wei, M.H. Ervin, S.O. Hruszkewycz, M.K. Miller, T.C. Hufnagel and K.T. Ramesh, Scripta Mater. 57 (2007) p.517.

[9] H. Guo, P.F. Yan, Y.B. Wang, J. Tan, Z.F. Zhang, M.L. Sui and E. Ma, Nature Mater. 6 (2007) p.735.

[10] D. Jang and J.R. Greer, Nature Mater. 9 (2010) p.215.

[11] C.C. Hays, C.P. Kim and W.L. Johnson, Phys. Rev. Lett. 84 (2000) p.2901.

[12] D.C. Hofmann, J.Y. Suh, A. Wiest, G. Duan, M.L. Lind, M.D. Demetriou and W.L. Johnson, Nature 451 (2008) p.1085.

[13] D.C. Hofmann, J.Y. Suh, A. Wiest, M.L. Lind, M.D. Demetriou and W.L. Johnson, PNAS 105 (2008) p.20136.

[14] F.F. Wu, Z.F. Zhang, A. Peker, S.X. Mao, J. Das and J. Eckert, J. Mater. Res. 21 (2006) p.2331.

[15] F.F. Wu, Z.F. Zhang, A. Peker, S.X. Mao and J. Eckert, Phys. Rev. B 75 (2007) p.134201.

[16] J.S. Park, H.K. Lim, J.H. Kim, J.M. Park, W.T. Kim and D.H. Kim, J. Mater. Sci. 40 (2005) p.1937.

[17] Y. Xiang, T. Li, Z.G. Suo and J.J. Vlassak, Appl. Phys. Lett. 87 (2005) p.161910.

[18] N. Lu, X. Wang, Z. Suo and J. Vlassaka, J. Mater. Res. 24 (2009) p.379.

[19] T.H. Fang, W.L. Li, N.R. Tao and K. Lu, Science 20 (2011) p.1587.

[20] A. Donohue, F. Spaepen, R.G. Hoagland and A. Misra, Appl. Phys. Lett. 91 (2007) p.241905.

[21] Y.M. Wang, J. Li, A.V. Hamza and T.W. Barbee, PNAS 104 (2007) p.11155.

[22] R.G. Hoagland, J.P. Hirth and A. Misra, Philos. Mag. A 86 (2006) p.3537.

[23] A.S. Argon, Acta Metall. 27 (1979) p.47.

[24] F. Spaepen, Acta Metall. 25 (1977) p.407.

[25] F. Spaepen and D. Turnbull, Scripta Metall. 8 (1974) p.563.

Figures Caption

Figure 1. (a), Schematic illustration of the preparation process of MGC/CPT bimetallic composites by argon-arc re-melting. (b,c), Optical microscope images showing the microstructure of the MGC/CPT bimetallic composite. (d) SEM image displays the microstructure of the MGC/CPT bimetallic composite. (e) X-ray pattern showing the body-centred cubic structure of the β-dendrites and the amorphous state of the matrix in the MGC/CPT removed from the CPT substrate.

Figure 2. (a) Engineering stress-strain curves for the monolithic MGC sample (S1), the CPT-confined MGC sample (S2), and the monolithic CPT sample, respectively. The inset indicates the tensile specimens after plastic deformation and fracture for S1 and S2. Sample S1 displays fully strain localization with remarkable necking, but S2 deforms homogeneously without obvious necking. (b) True stress-strain curve for the CPT-confined MGC sample S2.

Figure 3. (a) Macroscopic SEM image showing the tensile sample S2 after plastic deformation and fracture. (b,c) Microscopic SEM images showing the deformation features in two typical regions of the MGC layer, which are marked as B and C in Fig. 3a. (d) Macroscopic SEM image showing the deformation features of the lateral surface of sample S2. (e) Enlarged image displaying the deformation features near the interface of S2, as marked in Fig. 3d. The up-down arrows show the tensile loading direction.

Figure 4. (a) Four deformation regions in the stress-strain curves of MGC/CPT: I, elastic region; II, CPT yielding region; III, MGC/CPT yielding and homogeneous deformation region; and IV, inhomogeneous deformation region. (b,c,d) Typical enlarged stress-strain curves segment marked as B, C, and D in Fig. 4a, respectively.

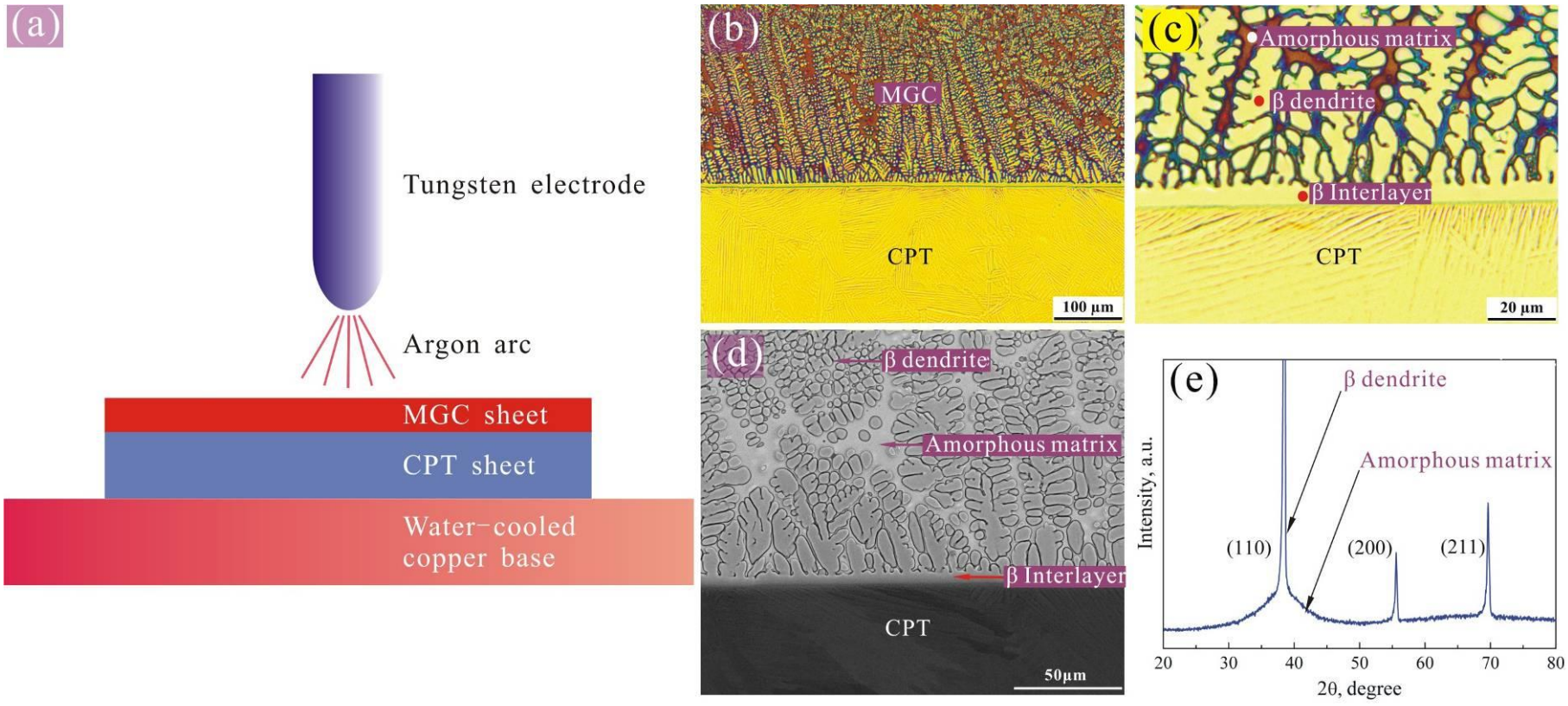
(a)
Tungsten electrode
Argon arc
MGC sheet
CPT sheet
Water-cooled copper base
(b)
MGC
CPT
100 μm
(c)
Amorphous matrix
β dendrite
β Interlayer
CPT
20 μm
(d)
β dendrite
Amorphous matrix
β Interlayer
CPT
50μm
(e)
β dendrite
Amorphous matrix
(110)
(200)
(211)
Intensity, a.u.
20
30
40
50
60
70
80
2θ, degree

Figure 1

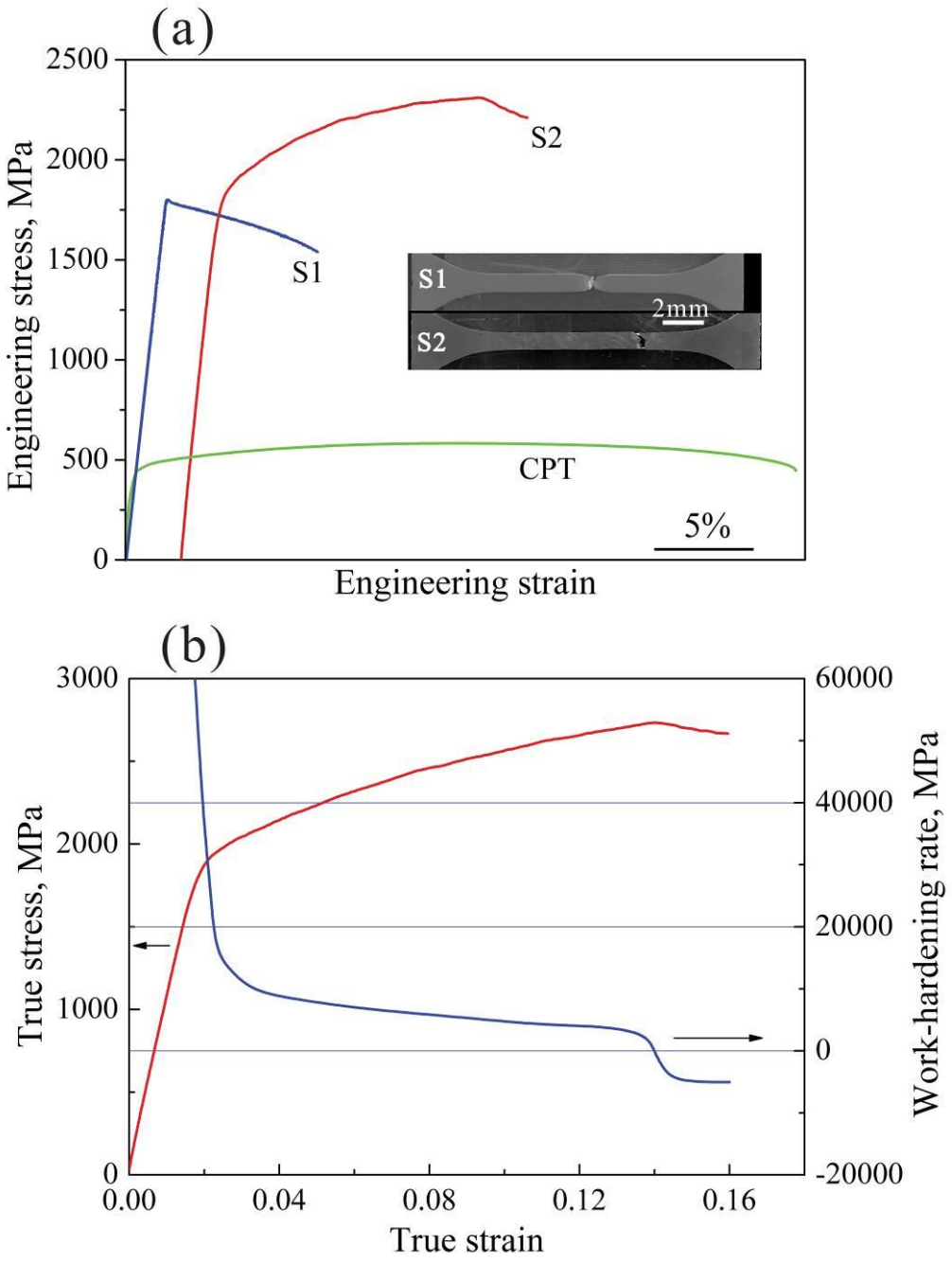
(a)
2500
2000
1500
1000
500
0
Engineering stress, MPa
S2
S1
S1
2mm
S2
CPT
5%
Engineering strain
(b)
3000
2000
1000
0
True stress, MPa
60000
40000
20000
0
-20000
Work-hardening rate, MPa
0.00
0.04
0.08
0.12
0.16
True strain

Figure 2

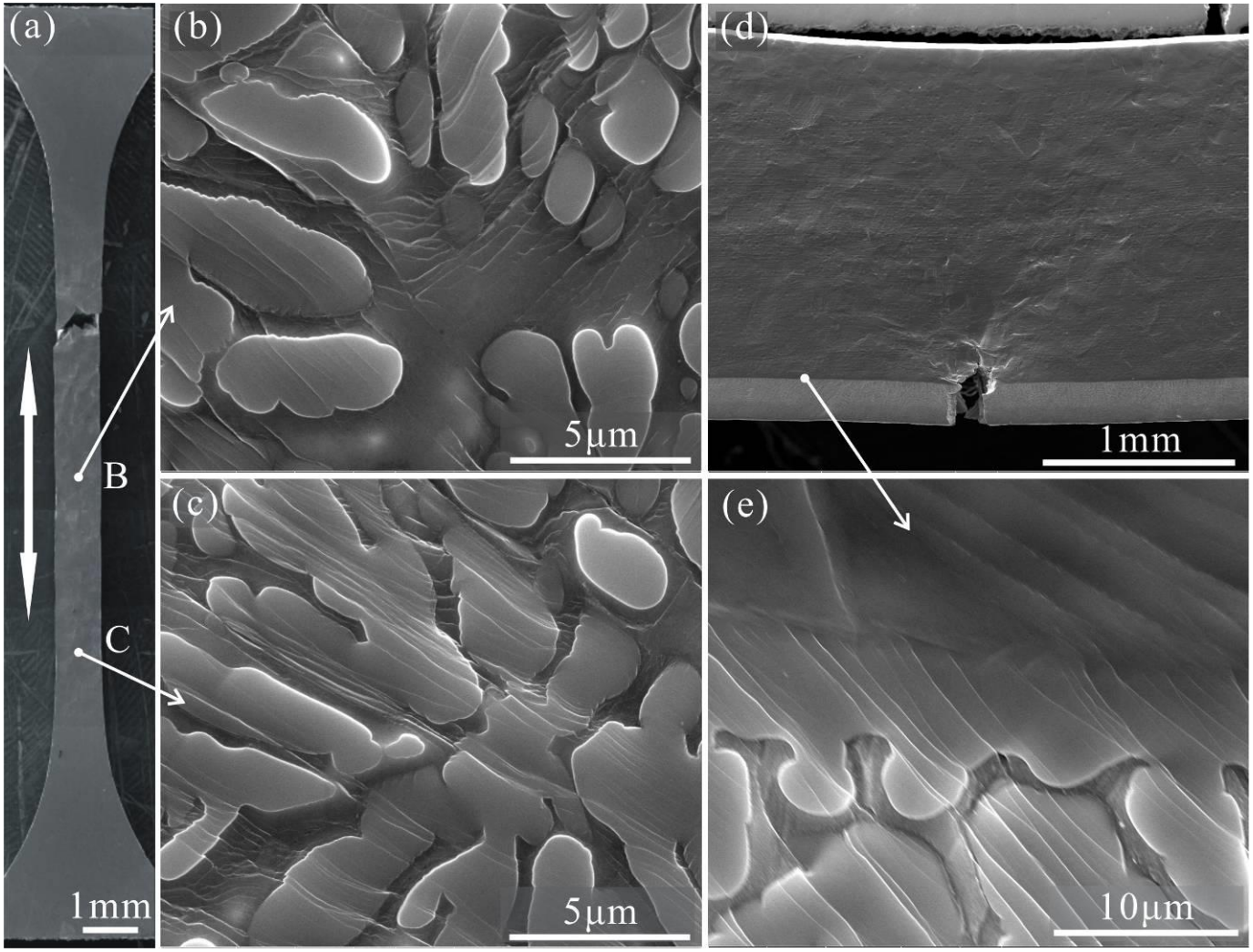

Figure 3

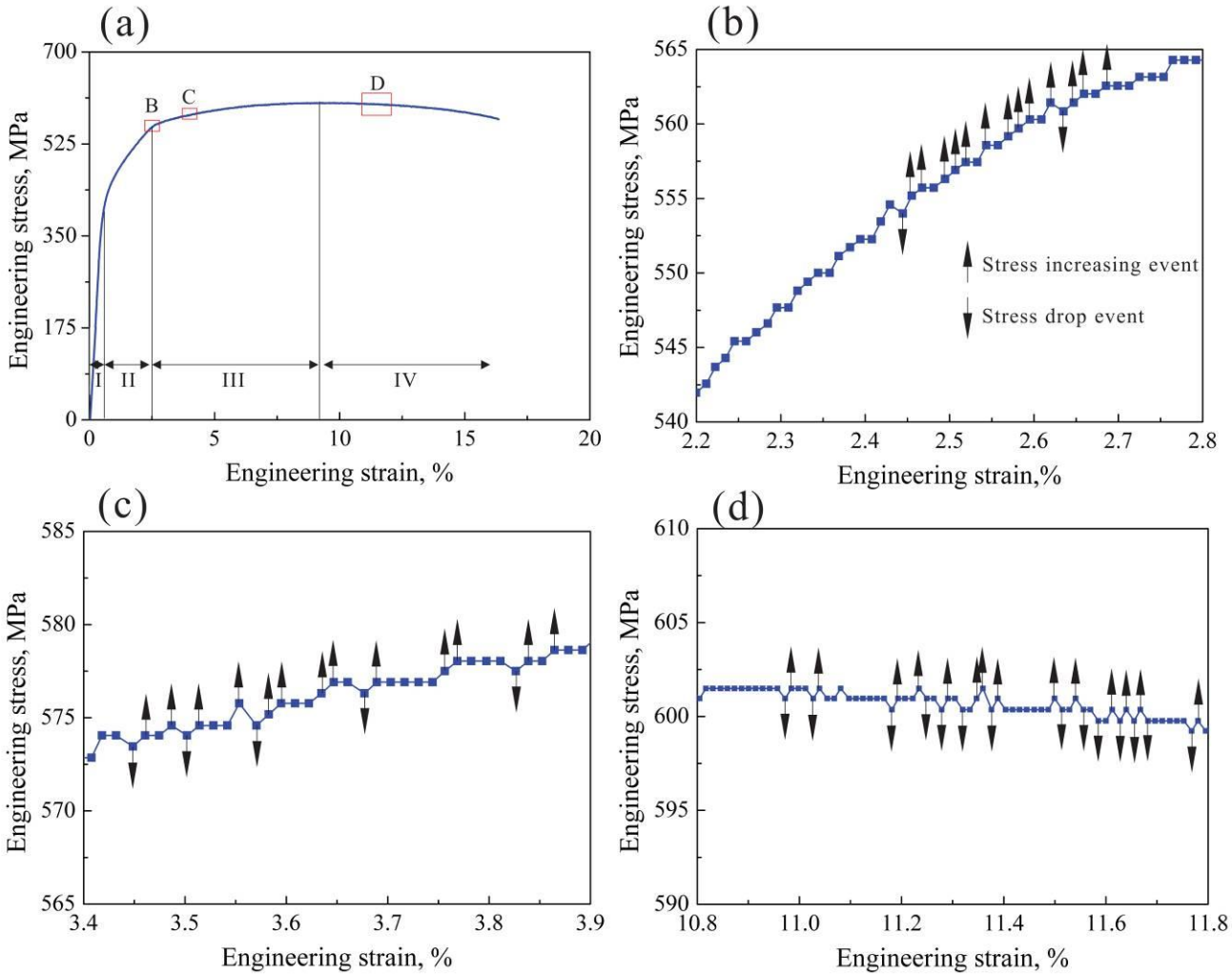
(a)
Engineering stress, MPa
Engineering strain, %
B
C
D
I
II
III
IV
(b)
Engineering stress, MPa
Engineering strain,%
Stress increasing event
Stress drop event
(c)
Engineering stress, MPa
Engineering strain, %
(d)
Engineering stress, MPa
Engineering strain, %

Figure 4